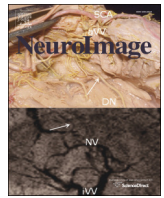




Contents lists available at ScienceDirect

NeuroImage

journal homepage: www.elsevier.com/locate/ynimg

Functional ultrasound imaging reveals different odor-evoked patterns of vascular activity in the main olfactory bulb and the anterior piriform cortex

Q1 B.F. Osmanski^a, C. Martin^b, G. Montaldo^a, P. Lanièce^b, F. Pain^b, M. Tanter^{a,1}, H. Gurden^{b,*,1}

^a Institut Langevin, ESPCI ParisTech, CNRS UMR7587, Inserm U979, Université Paris 7, France

^b Laboratoire IMNC, CNRS UMR8165, Université Paris Diderot 7 et Université Paris Sud, France

ARTICLE INFO

Article history:

Accepted 11 March 2014

Available online xxxx

Keywords:

Piriform cortex

Functional ultrasound imaging

Blood volume

Odor activation

ABSTRACT

Topographic representation of the outside world is a key feature of sensory systems, but so far it has been difficult to define how the activity pattern of the olfactory information is distributed at successive stages in the olfactory system. We studied odor-evoked activation patterns in the main olfactory bulb and the anterior piriform cortex of rats using functional ultrasound (fUS) imaging. fUS imaging is based on the use of ultrafast ultrasound scanners and detects variations in the local blood volume during brain activation. It makes deep brain imaging of ventral structures, such as the piriform cortex, possible. Stimulation with two different odors (hexanal and pentylacetate) induced the activation of odor-specific zones that were spatially segregated in the main olfactory bulb. Interestingly, the same odorants triggered the activation of the entire anterior piriform cortex, in all layers, with no distinguishable odor-specific areas detected in the power Doppler images. These fUS imaging results confirm the spatial distribution of odor-evoked activity in the main olfactory bulb, and furthermore, they reveal the absence of such a distribution in the anterior piriform cortex at the macroscopic scale *in vivo*.

© 2014 Elsevier Inc. All rights reserved.

Q2 Introduction

Processing of olfactory information is vital for the majority of vertebrates. The olfactory system is built in the same scheme across species, with only two synaptic relays to reach the olfactory cortex from the outside world (Bekkers and Suzuki, 2013). The wiring diagram of the olfactory circuits starts with the olfactory receptor neurons (ORNs), located in the main olfactory epithelium. In the rodent, each ORN, expressing one particular olfactory receptor out of ~1000 (Firestein, 2001; Mombaerts, 2004; Mori and Sakano, 2011), projects out to four glomeruli in the main olfactory bulb (MOB), the first central relay that codes the olfactory information (Shepherd and Greer, 1998). In turn, the MOB transmits the information to the anterior piriform cortex (aPC), the main output structure of the MOB among the primary olfactory cortices. The aPC receives direct and dense sensory input from the mitral/tufted cells (M/TCS) in the MOB from multiple glomerular sources through the lateral olfactory tract (LOT) projection (Apicella et al., 2010; Miyamichi et al., 2011). In addition, different tracing

techniques have been used to show that M/TC axons from individual glomeruli were diffusely projecting throughout the aPC (Ghosh et al., 2011; Miyamichi et al., 2011; Sosulski et al., 2011).

Odor-induced spatial maps of the MOB have been characterized extensively (Mori et al., 2006; Murthy, 2011), in particular by *in vivo* optical imaging (Uchida et al., 2000) and magnetic resonance imaging (MRI) (Xu et al., 2000). A given odorant molecule can activate various subsets of ORNs, which results in a spatially invariant pattern of glomerular activity in the MOB (Belluscio and Katz, 2001; Soucy et al., 2009). Physiological studies have examined the transmission of odor-evoked activities from the MOB to the aPC (Litaudon and Cattarelli, 1996; Poo and Isaacson, 2009; Rennaker et al., 2007; Stettler and Axel, 2009; Suzuki and Bekkers, 2012). These studies have shown that odorants activate sparse groups of neurons that are largely distributed in all layers of the aPC, without any apparent spatial preference. However, it is not known how odor-evoked activation of different odors is organized in the aPC at the macroscopic scale.

In this study, we used functional ultrasound (fUS) imaging (Macé et al., 2011), a new functional neuroimaging technique based on the use of ultrafast ultrasound scanners, to map odor-evoked activity in the aPC on a large scale. Ultrafast ultrasound scanners have already offered new insights in diagnostic imaging (Tanter et al., 2008) and blood flow imaging under the terminology of “Ultrafast Doppler Imaging” (Bercoff et al., 2011; Osmanski et al., 2012; Udesen et al., 2008). This concept relies on compounded plane wave transmission

Abbreviations: ORNs, olfactory receptor neurons; fUS, functional ultrasound; MOB, main olfactory bulb; aPC, anterior piriform cortex.

* Corresponding author at: Laboratoire IMNC, CNRS UMR8165, Université Paris Diderot et Université Paris Sud. 91405 Orsay, France. Tel.: +33 169154509.

E-mail address: gurden@imnc.in2p3.fr (H. Gurden).

¹ Last co-authors.

(Montaldo et al., 2009), which can capture more than 10,000 frames per second compared to the usual 50 frames per second in conventional ultrasound scanners. Thus, Ultrafast Doppler has increased the sensitivity of blood flow measurements by 30-fold (Macé et al., 2013), making the detection of subtle hemodynamic changes in smaller vessels possible compared to conventional Doppler Ultrasound. Similar to other magnetic and optical functional neuroimaging techniques that depend on vascular oxygenation and dynamics (Pain et al., 2011), fUS relies on activity-dependent blood volume changes in small blood vessels to detect active neuronal assemblies in vivo (Macé et al., 2013; Rubin et al., 1995, 1997; Shung et al., 1976). Importantly, fUS was shown to reach an excellent spatiotemporal resolution (below 100 μm and 1 s for a single trial acquisition) in the field of deep brain imaging (Macé et al., 2011).

Using the technical advantages of fUS, we determined how distinct odorants were mapped in two interconnected stations along the olfactory pathway, the MOB and the aPC, on a macroscopic scale. We confirmed the existence of the well-described spatial maps evoked by odor stimulation in the MOB, and we further showed that the aPC is activated as a whole, across all layers, in response to different odorants.

Materials and methods

Animals, surgical procedures and odor delivery

Thirteen adult male Long–Evans rats (Janvier Labs; France) weighing 250–350 g were included in this study. They were housed in collective cages with free access to food and water and maintained under standard conditions (12/12 h light–darkness cycle, 22 °C). All experiments were conducted in accordance with the European Community Council Directive (86/609/EEC). The experimental protocol was controlled and approved by the University Paris-Sud Ethics Committee and the Direction of Veterinary Service (authorization #B91471101).

All rats were anesthetized by an intraperitoneal (i.p.) injection of a mixture of ketamine (60 mg/kg, Imalgene 500®, Merial; France) and medetomidine (0.4 mg/kg, Domitor®, Pfizer Santé Animale; France). Anesthesia was maintained by a periodic i.p. dosage using 1/3 of the initial dose. Body temperature was monitored and maintained at 37 °C using a heating blanket throughout the experiment. Animals were placed in a stereotaxic apparatus for imaging. After an incision in the cranial skin, the bone above the MOB or the aPC was thinned by a dental drill and carefully removed. All image recordings were conducted on freely breathing rats (constant breathing at 1–2 Hz in all rats).

A custom-modified version of a multivial perfusion system (ValveBank 8 II, AutoMate Scientific; USA) attached to an air compressor was used as an olfactometer. A precise volume of the diluted odor (50 μL) was loaded onto a filter paper and placed in a syringe reservoir. Pressure controlled air was delivered through the perfusion system, ensuring a constant rate of odorized air to the animal's nose during valve opening. A mask was placed in front of the rat's nostrils to deliver the odors.

A single activation trial lasted for 48 s. After 6 s of baseline recording under a constant deodorized airflow, one of the two odorants, hexanal 1% or pentylacetate 1% (Sigma-Aldrich; USA), was delivered for 15 s. Another 27 s of air delivery was allowed to recover the baseline value of the metabolic signal. Because the olfactory system is very sensitive to desensitization habituation in the case of repetitive odor stimulations, we allowed at least 3 min of inter-trial interval (ITI). Blank trials, with only air delivered throughout the 48 s, were performed between the odor trials. Four trials per odor were averaged together to obtain functional images of the MOB and the aPC.

To build a recording chamber for each structure, craniotomies were performed according to the MOB and aPC stereotaxic coordinates (Paxinos and Watson, 2007). In a group of five rats, a 5 mm window from 6.5 to 9.5 mm anterior to the bregma was made to give access to the entire MOB. In another group of 8 rats, a 10 mm window was

made from 3 to 5 mm anterior to the bregma to give access to the aPC. A silicone gel was applied to the surface of the dura. The gel allows perfect coupling between the ultrasonic probe and the imaged brain region and makes the propagation of ultrasound wave fronts possible. Anteroposterior scans were performed, placing the ultrasound probe on top of these two regions (Fig. 1A). The choice of the ultrasonic image slice with the maximal signal to noise for the power Doppler signal was made taking the shape of the vasculature as a reference (see Fig. 2).

In vivo fUS: images and statistical analysis

fUS was performed using a linear ultrasound probe (192 elements, 20 MHz, 80 μm pitch, and 8 mm elevation focus, Vermon; France) driven by an ultrafast ultrasound scanner (Aixplorer, Supersonic Imagine; France). The biophysics and the technical procedure for fUS were fully explained in our previous reports (Macé et al., 2011, 2013). Briefly, to obtain an ultrasound image of the brain tissue, we used the following ultrafast imaging fUS sequence: i) insonify the brain tissue with a plane wave, ii) record the backscattered echoes coming from a wide-field view on the transducer array, and iii) beamform the raw data to produce an image. In order to ensure a high-quality ultrasound image while preserving an ultrafast frame rate (several 100 s of frames per second), we added several plane wave images coherently (with amplitude and phase) from successive transmissions of tilted plane waves (Montaldo et al., 2009). In this study, the plane wave compounding consisted of coherently adding the images of the brain tissue from 15 different tilted plane waves, with angles varying from -7° to 7° and a 1° step, to compute one high-quality ultrasound image (Fig. 1B). To sample blood flow changes, we repeated this sequence 200 times with a 500 Hz frame rate (corresponding to a 400 ms acquisition time) (Fig. 1C). Because blood moves faster than the tissue, its signal is higher in frequency and can be extracted by time filtering the data with a high-pass filter (4th order Butterworth with a 75 Hz cutoff). One image of power Doppler intensity (which is proportional to the cerebral blood volume, CBV) is obtained by the incoherent temporal mean of the blood signal. Because of the technological computing limitations of our fUS platform (6 CPU core unit, 24 GB RAM), a dead time of 1.1 s is needed to process the power Doppler signal (beamforming and high-pass filtering), resulting in a final temporal sampling rate of 1.5 s per image (Fig. 1D). At the end of this signal processing, we reliably recorded CBV variation in the imaging plane.

Maps of activated pixels were built showing the normalized correlation coefficient r between the local power Doppler signal obtained from fUS and the temporal binary pattern of the odor stimulus. Activation was considered significant for a correlation $r > 2\sigma$, where σ is the spatial standard deviation of the correlation map linked to the noise of the fUS technique. As the volume imaged by fUS covers more than just the brain tissue, σ was computed using at least 100 pixels of the correlation map located outside of the brain. Therefore, this thresholding method can be considered independent of brain activity. The time course for a given region was calculated by averaging the power Doppler signal over time for all pixels in the activated region ($r > 2\sigma$). The intensity of the power Doppler was represented as the percentage of change relative to the baseline in the activated region \pm standard deviation (STD). Finally, raw (i.e., not thresholded) hexanal and pentylacetate activation maps in the aPC were compared using the Pearson correlation coefficient.

Results

fUS imaging in the olfactory system

In this study, we investigated the odor-evoked activation of the MOB and the aPC using the fUS technique. We achieved a spatial resolution of 100 μm \times 100 μm in the imaging plane, with a slice thickness of 300 μm and a penetration depth (>2 cm) sufficient to image deep brain

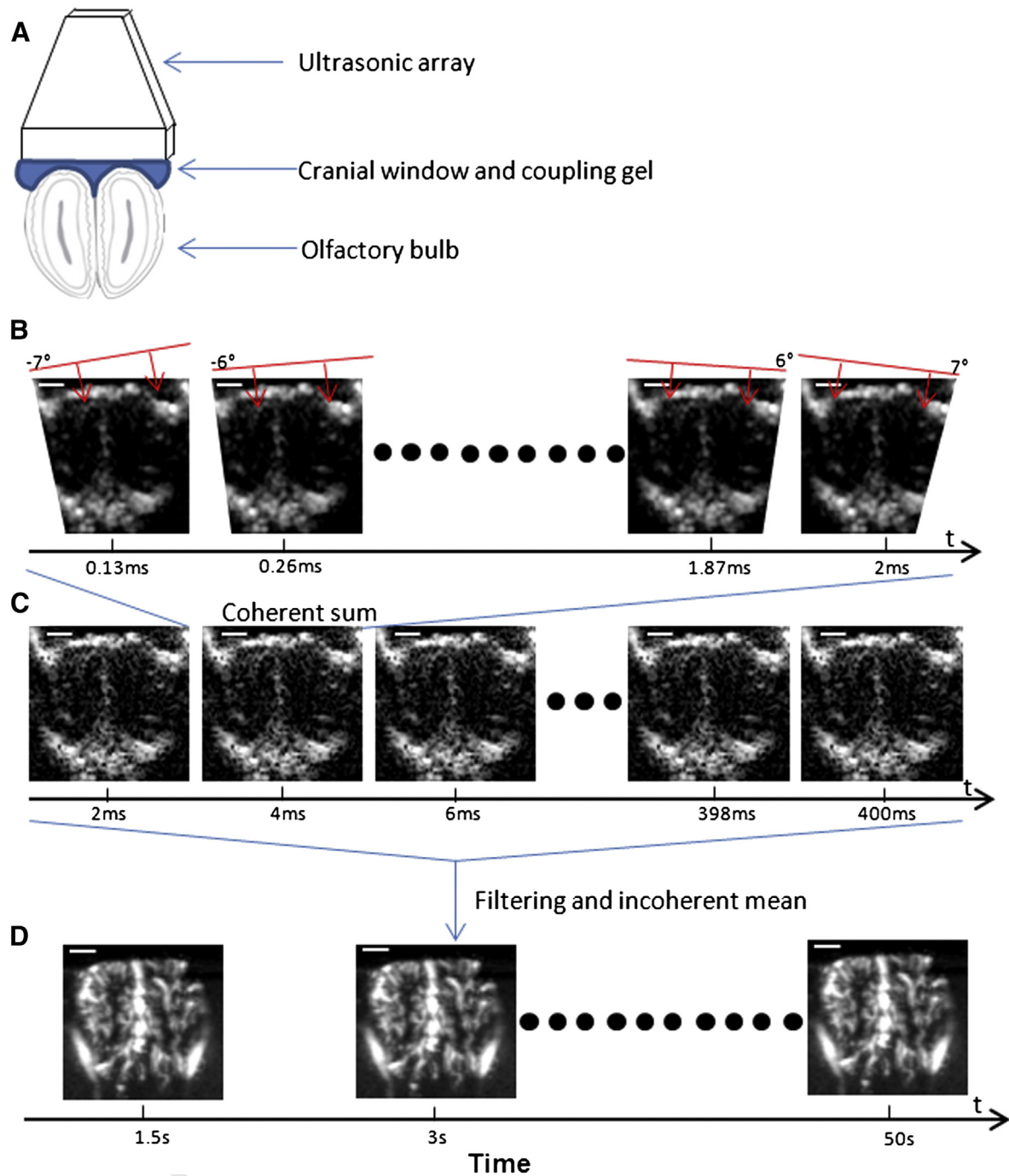


Fig. 1. Protocol for fUS imaging. (A) Experimental setup. The ultrasound probe is placed on top of the MOB after removal of the skull bone. The gel allows for perfect coupling between the ultrasonic probe and the tissue. (B) Plane wave insonification of the brain tissue, with angles varying from -7° to 7° and a 1° step, is performed to record 15 low quality images. After the coherent sum of these 15 images, one quality image of the brain tissue is produced. (C) Repetition of the compounded sequence 200 times with a 500 Hz frame rate results in one Doppler image. (D) One power Doppler intensity image is obtained every 1.5 s during 48 s to measure the spatiotemporal variations of the CBV. For further details see the [Materials and methods](#) section.

198 structures. Doppler scans were performed in the full anteroposterior ex- 208
 199 tent of each structure to observe the overall vascular network (Figs. 1 209
 200 and 2). Using these images as an anatomical reference, we determined 210
 Q3 the stereotaxic coordinates to record the fUS for both the MOB and the 211
 202 aPC in a series of preliminary experiments (images not shown). When 212
 203 we performed the actual fUS recording included in our study, we refined 213
 204 the anteroposterior location of the probe to maximize the power 214
 205 Doppler signal. We then probed the odor-evoked vascular activity in 215
 206 a single slice from each structure. To the best of our knowledge, we 216
 207 have produced the first fUS images of the MOB and aPC using in vivo

208 imaging of CBV changes, which permitted us to assess the spatial distri- 209
 210 bution of the odorant-activated areas in the MOB and the aPC in anes- 211
 212 thetized rats. 213

Odor-evoked activation of the MOB 211

212 First, we visualized the vasculature in the MOB, where dense vascular 213
 214 inputs can be observed at the glomerular level (Fig. 2A). Blank trials 215
 216 where only air was delivered to the animal showed no specific activity 217
 in the MOB (Fig. 3A). We next mapped specific odor-activated zones 218

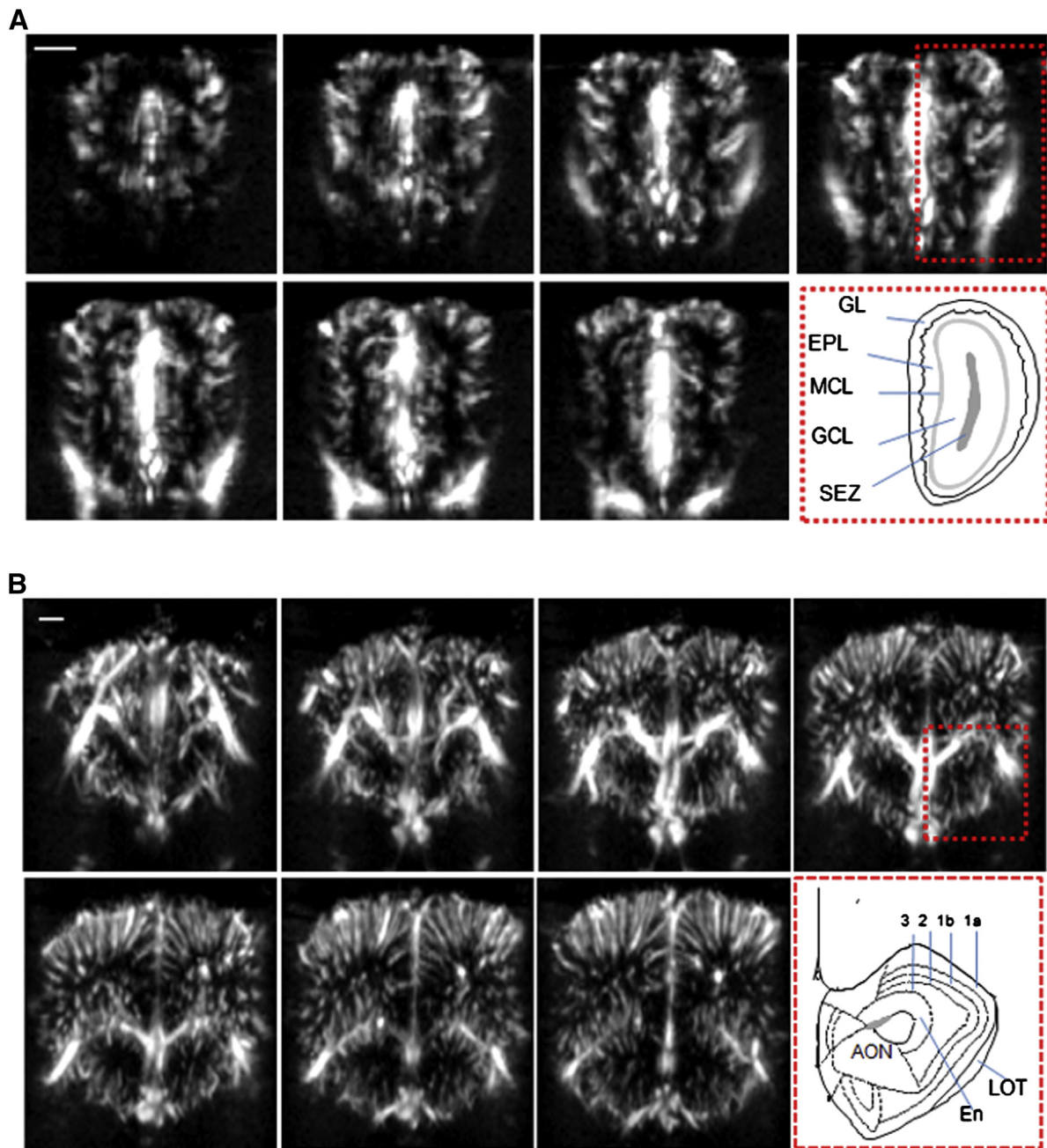


Fig. 2. MOB and aPC vasculature visualized by fUS on 0.3 mm thick coronal slices acquired in the antero-posterior axis (from left to right) in one rat. (A) A dense vascular input is observed in superficial layers of the MOB and decreases in the inner zones. Each image is made with one power Doppler intensity acquisition. The horizontal white bar represents 1 mm. EPL: external plexiform layer. GL: glomerular layer; GCL: granule cell layer; MCL: mitral cell layer; SEZ: subependymal zone. (B) A dense vascular input is observed in all three layers of aPC. The horizontal white bar represents 1 mm. AON: anterior olfactory nucleus. 3, 2, 1b, 1a: layers of aPC. En: endopiriform nucleus. LOT: lateral olfactory tract. Anatomical schemes in (A) and (B) modified from Paxinos and Watson (2007).

(Figs. 3B–D). Artifacts due to respiratory or cardiac movements in the preparation or to spontaneous variation in the vascular activity occasionally occurred during the recordings, but they were efficiently removed from the fUS image using the average of four trials as they happen asynchronously with respect to the stimulus. Interestingly, even one trial was able to produce significant changes enough to allow observation of the power Doppler signal over the background noise in the MOB, as well as record the spatial distribution of activation (Figs. 3B–C). We averaged four trials to obtain an activation map, in an effort to normalize the variability in the reactive areas to odorants that may change from trial to trial (see for example the ventral part of the

MOB in response to hexanal in Fig. 3B). We found that both odorants induced specific and symmetrical maps in the MOB (Figs. 3B–C). Hexanal induced further dorsal MOB activity over pentylacetate, which recruited lateral and ventral areas of the MOB when visualized in the same rat (Fig. 3D). Each of the images acquired in Figs. 3B–D is from an independent, representative rat. The odor-evoked power Doppler onset was locked to odor delivery and occurred within 3.00 ± 0.75 s ($n = 5$) after the stimulus onset for both odorants (Fig. 3E). The power Doppler time course was monophasic, meaning that it reached a single peak at 4.50 ± 0.75 s after the odor onset and then returned to baseline. The amplitude of the power Doppler peak relative to the baseline was 12 ± 27

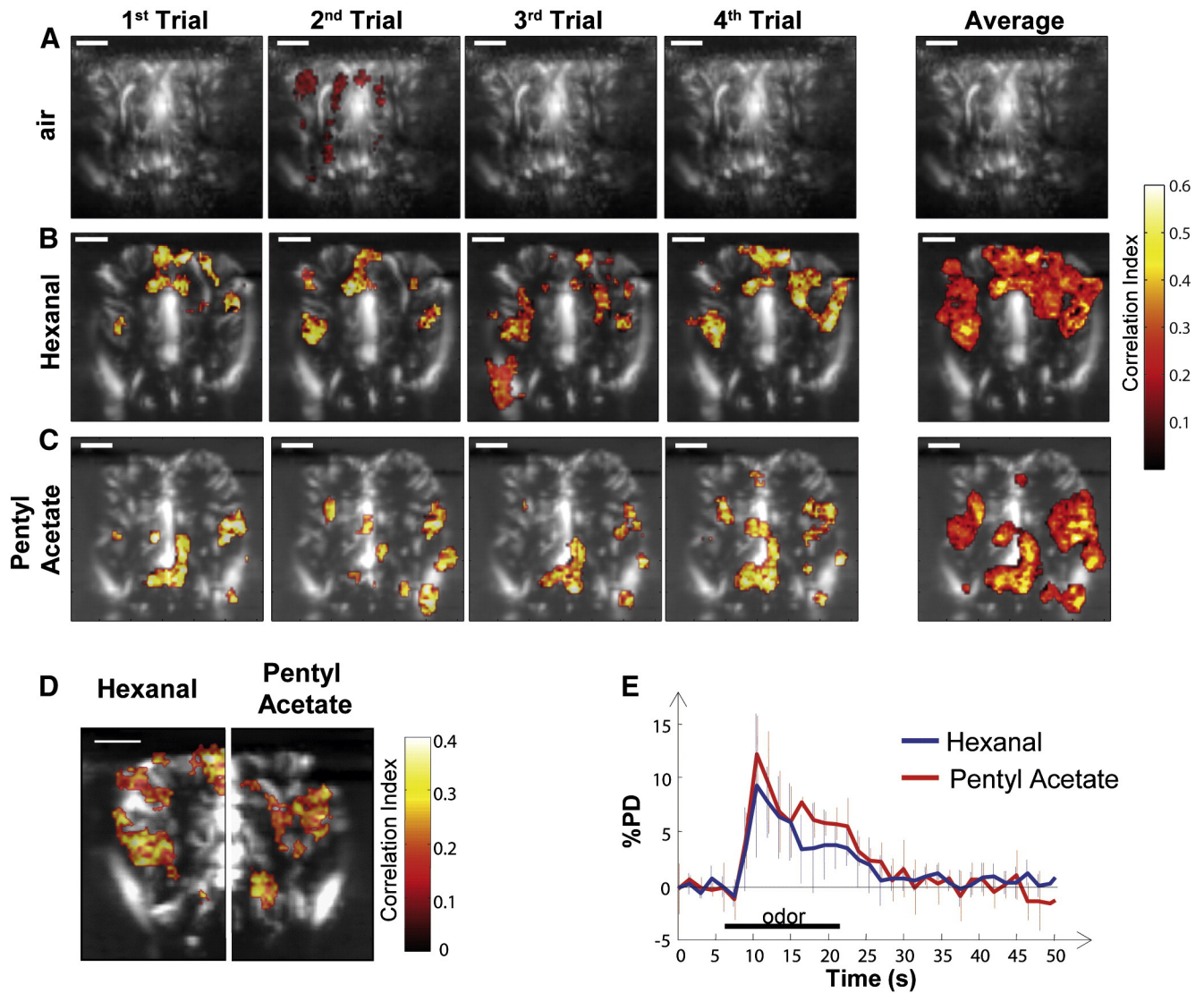


Fig. 3. fUS imaging of odor-evoked activity in the MOB for two different odors. (A) Blank trials in a representative rat. Air stimulation was delivered during the 48 s trial. Four independent trials and the average of these trials are represented. Note that occasionally vascular artifacts occur. The computing of the final correlation map of these four blank trials efficiently excludes these artifacts. (B) Spatial distribution of activity elicited by odor presentation in the MOB for hexanal 1% in a representative rat. The olfactory map is characterized by a precise spatial location and a symmetrical distribution in this coronal view. The horizontal white bar represents 1 mm. (C) Spatial distribution of activity elicited by odor presentation in the MOB for pentyl acetate 1% in one rat that was different from the hexanal trials. B–C, same representation as (A). The horizontal white bar represents 1 mm. (D) Comparison of olfactory maps triggered by the two odorants in the same representative rat. Note that hexanal-induced signals are more dorsal than the pentylacetate-induced ones. Each image is the average of four odor trials acquired in the same rat (different from the rats shown in B and C). The horizontal white bar represents 1 mm. (E) Time course of sensory-evoked activity in the MOB. Both odors induce the same power Doppler dynamics in terms of time course and amplitude. Each curve is the average of four odor trials ($n = 5$ rats).

238 3% and $10 \pm 6\%$ for pentylacetate ($n = 5$) and hexanal ($n = 5$, same
239 animal as with the pentylacetate), respectively (Fig. 3E).

240 Odor-evoked activation of the aPC

241 Our modified fUS technique also made it possible to record aPC activation.
242 Dense vascular inputs can be visualized in the three layers of the
243 aPC (Fig. 2B). Functional images are represented in Fig. 4, which has the
244 same format as Fig. 3. aPC did not present a patchy pattern of activation
245 in response to the different odorants. On the contrary, we always
246 observed a global, widespread odor activation that covered all of
247 the layers (Figs. 4B–E). Each of the images acquired in Figs. 4B–D is
248 from an independent, representative rat. In the aPC, the hexanal and
249 pentylacetate maps were highly correlated (Pearson correlation coefficient
250 = 0.53 ± 0.08 , $p < 0.001$, $n = 8$), meaning that the aPC maps for
251 these odorants highly overlapped. The odor-evoked Doppler onset in
252 the aPC was locked to odor delivery and occurred within 3.00 ± 0.75 s

($n = 8$) after the stimulus onset for both odorants (Fig. 4E). The
253 power Doppler time course recorded in the aPC presented multiple
254 peaks of activity. The first peak occurred within 4.5 ± 0.75 s after
255 the odor onset for both stimuli ($n = 8$, same rats used for both hexanal
256 and pentylacetate, Fig. 4E). It reached a normalized amplitude of
257 $5 \pm 2\%$ and $7 \pm 3\%$ for pentylacetate ($n = 8$) and hexanal ($n = 8$),
258 respectively. The second peak occurred at 18 ± 0.75 s for pentylacetate
259 ($n = 8$) and 19.5 ± 0.75 s for hexanal ($n = 8$ same rats used in both
260 experiments) after odor onset (Fig. 4E), with a normalized amplitude
261 of $6 \pm 3\%$ for pentylacetate ($n = 8$) and $7 \pm 2\%$ for hexanal ($n = 8$)
262 (Fig. 4E).
263

264 Discussion

265 Understanding how the functional connectivity to higher order sensory
266 processing regions is distributed has profound implications for the way
267 that odors are perceived. Recent work has revealed that odors are

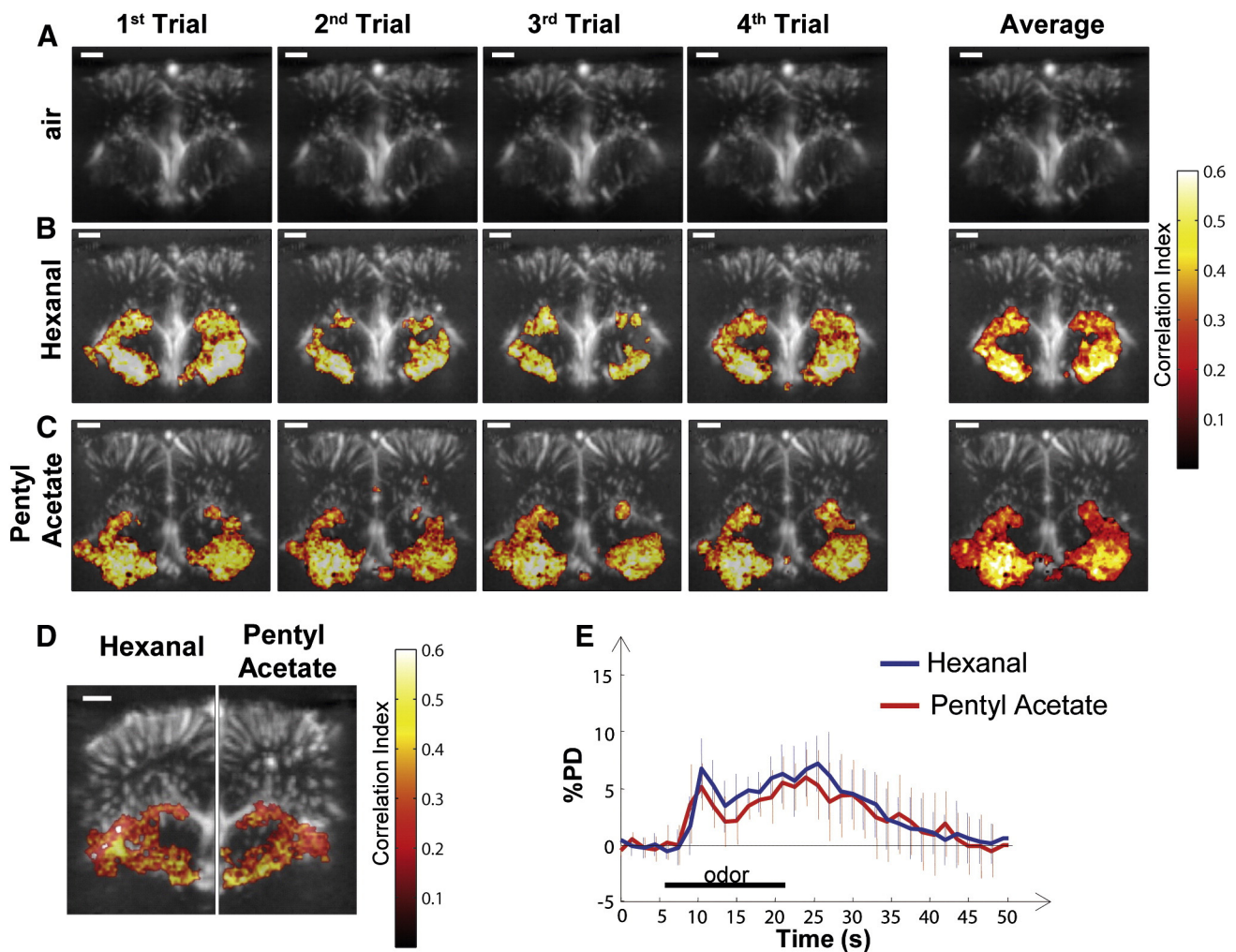


Fig. 4. fUS imaging of odor-evoked activity in the aPC for two different odors. (A) Blank trial in a representative rat. Same representation as in Fig. 3A. (B) Spatial distribution of activity elicited by odor presentation in the aPC for hexanal 1% in a representative rat. Note the absence of any specific zone of activity compared to MOB mapping in Fig. 3B. (C) Spatial distribution of activity elicited by odor presentation in the aPC for pentylacetate 1% in one rat (different rat from the hexanal trials). Note that the distribution of activity highly overlaps between the hexanal and pentylacetate treatments. The horizontal white bar represents 1 mm. (D) Spatial distribution of activity elicited by odor presentation in the aPC for hexanal 1% and pentylacetate 1% in one representative rat. All layers of the aPC are diffusely activated by the two odorants. Each image is the average of four odor trials in the same rat (different from the rats shown in B and C). The horizontal white bar represents 1 mm. (E) Both odors induce the same power Doppler dynamics in the aPC. In contrast to MOB activation, the aPC time course is characterized by multiple peaks of activity. Each curve is the average of four odor trials ($n = 8$ rats).

268 sparsely represented in the aPC, at the level of a single neuron (Poo and
 269 Isaacson, 2009; Stettler and Axel, 2009). Using fUS to probe activation at
 270 the macroscopic level, we demonstrated that the spatial organization in
 271 the MOB is not conserved in the aPC; activation in the aPC is widespread
 272 in response to an odor and not distinguishable between different odors.

273 *fUS imaging technique: a new tool to sample activity-dependent vascular*
 274 *changes in the brain*

275 fUS is a new technique that was used to visualize the activation of
 276 the somatosensory cortex in response to paw stimulation (Macé et al.,
 277 2011). An exhaustive review on the advantages and limitations of fUS
 278 imaging has recently been published (Macé et al., 2013). The following
 279 are the main points to consider with this technique, in the context of
 280 olfactory imaging.

281 The spatial resolution of the fUS technique is the actual resolution of
 282 the ultrafast plane wave imaging. In ultrasound imaging, the lateral and
 283 the depth resolution correspond to the wavelength used for imaging. In
 284 our case, since the frequency was 15 MHz and the speed of sound was
 285 1540 m/s, the wavelength was 100 μm . Thus, the resolution in depth
 286 and in the lateral direction was 100 μm . The resolution in the ultrasound
 287 plane of ultrafast imaging (both lateral resolution and axial resolution)

288 does not vary with depth (Denarie et al., 2013; Montaldo et al., 2009).
 289 The resolution in the elevation plane is set by a geometrical focal
 290 acoustic lens and by the shape of the ultrasound wave field and could
 291 vary with depth. This resolution was measured and ranges between
 292 300 μm at the focal distance of the geometrical focal lens (8 mm from
 293 the probe) and 400 μm on the upper and lower edges of the imaging
 294 field. In order to optimize the slice thickness, the geometrical focus
 295 was placed in the middle of the MOB or the aPC.

296 For MOB imaging, the fUS spatial resolution (in-plane resolution
 297 100 * 100 μm with a slice thickness of 300 μm) is comparable to Blood
 298 Oxygen Level Dependent (BOLD)-fMRI (200 * 200 μm with a slice thick-
 299 ness of 250 μm in Xu et al., 2000). However, compared to BOLD-fMRI,
 300 fUS provides easier access to a functional neuroimaging system, in
 301 terms of financial cost, portability (the fUS machine is transportable and
 302 installed on wheels), and technical combination (easier multimodality
 303 with electrophysiology, Macé et al., 2011). Owing to its penetration
 304 depth (>2 cm), fUS can record vascular signals from ventral cortices in
 305 the rodent brain, such as the aPC.

306 fUS does suffer from some limitations that can be overcome in the
 307 future. Similar to optical and MR imaging techniques using vascular
 308 signals, a central question is the compartmental origin of the power
 309 Doppler signal. The fUS signal is proportional to the number of moving
 310

red blood cells (RBCs) in the recorded voxel (Shung et al., 1976). The proportionality of the power Doppler signal to the blood volume (Rubin et al., 1995, 1997) is valid if the hematocrit is considered constant and if we disregard the possible variations in RBC backscattering properties. In theory, fUS could be sensitive to any moving objects that scatter from the brain tissue signal and/or from the blood. To specifically access hemodynamics, the signal coming from the brain tissue has to be subtracted with a high-pass filter (called clutter filtering in the ultrasound field). However, clutter filtering limits the signal from slow blood flow (RBCs with an axial velocity less than 4 mm/s are not recorded). Because two-photon fluorescence light microscopy imaging showed a velocity of 0.8 mm/s in the MOB (Chaigneau et al., 2003), which corresponds to the average capillary velocity (Kleinfeld et al., 1998), fUS cannot detect variations in blood vessels with slow dynamics, such as the capillary bed. Arterioles present a blood flow ten times superior to capillaries (Dirnagl et al., 1992; Petzold et al., 2008; Shih et al., 2009). Thus, fUS is particularly sensitive to hemodynamics in arterioles participating in functional hyperemia, defined as the matched increase in neuronal activity and local hemodynamics (Petzold and Murthy, 2011). For the time being, arterioles are the prime source for the power Doppler signal. As in other techniques dependent on blood dynamics, such as optical imaging and BOLD-fMRI (Kim and Ogawa, 2012), the cellular triggers and vascular origins of power Doppler signals must be further explored (Macé et al., 2013). In this context, the relationship between hematocrit and changes in CBV and CBF during sensory activation must also be explored.

Another issue with fUS, as in other imaging techniques, is signal processing. In this study, we efficiently proceeded with a thresholding technique that used a correlation method with a standard square-wave model based on the shape of the stimulus. With this type of processing, we obtained reproducible activation maps. Because the odor-evoked vascular response in the aPC has a complex shape (characterized by several peaks) and no model for aPC hemodynamics is available in the literature, we decided against using a more sophisticated thresholding method. In the close future, improvements in the signal processing of power Doppler signals are expected, with a better knowledge of hemodynamics in response to odors in the aPC. In particular, to suppress the 1.1 s dead time currently necessary for signal processing and to increase the temporal resolution in power Doppler signal acquisition, the new generation of high-end graphics processing unit boards will be incorporated into the future version of the fUS imaging set-up. This technical improvement will make the real-time processing of power Doppler signals and high temporal resolution for the follow-up of hemodynamics possible.

Presently, fUS requires anesthesia and a craniotomy. A craniotomy induces changes in the intracranial pressure that could impact the local vasculature. However, the intracranial pressure changes induced by local skull removal are not likely to significantly influence the sensory-evoked vascular signals since the olfactory maps recorded using IOS with a thinned bone overlying the MOB or without bone and dura have resulted in the same maps (Wachowiak and Cohen, 2003). In addition, in our experiments the dura was kept intact during fUS in the MOB and the aPC, and we could reliably record power Doppler signals in the dorsal MOB close to the site of the craniotomy (see Fig. 2B). Anesthesia partially inhibits vascular reactivity (Desai et al., 2011), as well as cellular mechanisms responsible for functional hyperemia (Thrane et al., 2012). However, neurovascular coupling is still present in acute preparations (Franceschini et al., 2010). Indeed, anesthetics are widely used in the olfactory field for imaging of vascular signals in vivo. Urethane (Lecoq et al., 2009; Petzold et al., 2008; Soucy et al., 2009; Xu et al., 2000), pentobarbital (Vincis et al., 2012; Wachowiak and Cohen, 2003), thiopental (Rubin and Katz, 1999; Uchida et al., 2000), and ketamine (Chery et al., 2011; Lecoq et al., 2009; Soucy et al., 2009) were successfully used to image the MOB and detected the same specific activated regions in response to the same odorants. Although we consider a ketamine-anesthetized preparation

appropriate for fUS imaging of the olfactory system, running non-invasive fUS imaging in awake, restrained rodents is clearly the next technical step.

Activation of odor-evoked spatial modules in the MOB recorded by fUS

fUS was previously used to image whisker-evoked cortical and thalamic responses in the rat brain (Macé et al., 2011). Here we recorded specific odor-activated zones in the MOB in response to two different odorants, confirming what has been shown by intrinsic optical signal imaging (Pain et al., 2011; Uchida et al., 2000) and fMRI (Xu et al., 2000) in vivo. For example, we observed that contrary to pentylacetate, hexanal activates the dorsal surface of the MOB. This is consistent with results found by other imaging techniques that studied MOB maps triggered by aldehydes such as hexanal (Johnson and Leon, 2000) versus acetates such as pentylacetate (Johnson et al., 1998). Therefore, our MOB images validate fUS for use in olfactory imaging. Furthermore, because (i) there is still much to understand about spatial coding of bulbar input to the aPC at the macroscopic scale and (ii) fUS has the advantage of sampling deep areas in the brain, we applied it to efficiently image aPC activation in response to different odorants in vivo.

Odor-evoked widespread vascular activity in aPC layers recorded by fUS

A topographic organization based on spatial domains is present in all sensory cortices of mammals. Spatial information in the peripheral sense organ is maintained by the cortex and has been demonstrated by several techniques, including optical and MR imaging. For example, whiskers are represented by maps within the barrels of the somatosensory cortex (Peterson, 2007), and there is a retinotopic organization of the visual cortex (Schuett et al., 2002). However, our data indicated a widespread increase in CBV in all aPC layers in response to different odorants. Thus, according to our results which complement previous data (Poo and Isaacson, 2009; Stettler and Axel, 2009), odor-evoked aPC representations differ from those of other neocortical sensory areas such as V1 or the barrel cortex, where cells are tuned for stimulus features and show macroscopic spatial patterning. It remains to be seen what the cellular origins of such a broad odor-evoked activation in the aPC could be.

Recurrent broadly distributed odor-evoked activity in the aPC at the macroscopic scale

The power Doppler signals that we recorded in the aPC presented a reverberating activity, with multiple peaks in all layers. Interestingly, the second peak of activity (~18 s after odor onset) occurred in the aPC long after the first one (~4 s after odor onset), which was concomitant with the single peak characterizing MOB activity. The odor-evoked time course of vascular activity recorded in the aPC could be due to the recurrent excitatory–inhibitory networks that were characterized within this structure (Franks et al., 2011; Poo and Isaacson, 2009). Anatomically, inputs from the MOB arrive through the LOT and make synapses with dendrites of the aPC cells in layer 1a (Bekkers and Suzuki, 2013; Haberly, 2001; Isaacson, 2010), whereas dense corticocortical association synapses are made in layer 1b (Bekkers and Suzuki, 2013; Haberly, 2001; Isaacson, 2010). Layers 2 and 3 contain the cell bodies of pyramidal cells (Bekkers and Suzuki, 2013; Haberly, 2001; Isaacson, 2010). Interneurons are present in all layers (Bekkers and Suzuki, 2013). Functionally, extracellular spike recordings have found that cells activated by a particular odor are distributed widely in the aPC (Litaudon et al., 2003; Rennaker et al., 2007). More recent studies have shown that a maximum of 15% of the pyramidal PC cells sampled with either patch clamp (Poo and Isaacson, 2009) or optical imaging (Stettler and Axel, 2009) is activated in response to an odorant. In addition, these recent studies revealed long-range excitatory connections to at least 2000 cells per cortical cell within the aPC. Therefore, this

extensive recurrent circuitry might be responsible for the global activity of the aPC. Still, global inhibition in the aPC (Franks et al., 2011; Poo and Isaacson, 2011; Suzuki and Bekkers, 2010, 2012; Zhan and Luo, 2010), which is broadly tuned, may also be responsible for the global activity detected in our fUS images: the fast spiking activity of inhibitory interneurons requires strong energetic inputs (Buzsáki et al., 2007) and specific classes of interneurons control local hemodynamics (Cauli et al., 2004). Describing the precise cellular mechanisms underlying fUS signals in the aPC, and particularly the role of inhibitory interneurons (Stokes and Isaacson, 2010; Suzuki and Bekkers, 2007), will be a major challenge for future fUS studies.

447 Conclusion

448 Using fUS to follow olfactory activation, we showed that the aPC
449 presents a widespread activation in response to different odors. fUS is
450 a technique well-suited to bring further insights to the understanding
451 of olfactory processing in the aPC. Further experiments are needed to
452 assess whether widespread activation of the aPC occurs for mixtures
453 of odorants (Stettler and Axel, 2009; Yoshida and Mori, 2007) and if
454 this activation may be refined with learning (Choi et al., 2011; Litaudon
455 et al., 2003; Saar and Barkai, 2009).

456 Q5 Uncited reference

457 Gurden et al., 2006

458 Conflict of interest statement

459 The authors have no conflict of interest to declare.

461 References

- 463 Apicella, A., Yuan, Q., Scanziani, M., Isaacson, J.S., 2010. Pyramidal cells in piriform cortex
464 receive convergent input from distinct olfactory bulb glomeruli. *J. Neurosci.* 30,
465 14255–14260.
- 466 Bekkers, J.M., Suzuki, N., 2013. Neurons and circuits for odor processing in the piriform
467 cortex. *Trends Neurosci.* 26, 429–438.
- 468 Belluscio, L., Katz, L.C., 2001. Symmetry, stereotypy, and topography of odorant represen-
469 tations in mouse olfactory bulbs. *J. Neurosci.* 21, 2113–2122.
- 470 Bercoff, J., Montaldo, G., Loupas, T., Savery, D., Mézière, F., Fink, M., Tanter, M., 2011. Ultra-
471 fast compound Doppler imaging: providing full blood flow characterization. *IEEE*
472 *Trans. Ultrason. Ferroelectr. Freq. Control* 58, 134–147.
- 473 Buzsáki, G., Kaila, K., Raichle, M., 2007. Inhibition and brain work. *Neuron* 56, 771–783.
- 474 Cauli, B., Tong, X.K., Rancillac, A., Serluca, N., Lambolez, B., Rössler, J., Hamel, E., 2004.
475 Cortical GABA interneurons in neurovascular coupling: relays for subcortical vasoac-
476 tive pathways. *J. Neurosci.* 24, 8940–8949.
- 477 Chaigneau, E., Oheim, M., Audinat, E., Charpak, S., 2003. Two-photon imaging of cap-
478 illary blood flow in olfactory bulb glomeruli. *Proc. Natl. Acad. Sci. U. S. A.* 100,
479 13081–13086.
- 480 Chery, R., L'Heureux, B., Bendahmane, M., Renaud, R., Martin, C., Pain, F., Gurden, H., 2011.
481 Imaging odor-evoked activities in the mouse olfactory bulb using optical reflectance
482 and autofluorescence signals. *J. Vis. Exp.* e3336.
- 483 Choi, G.B., Stettler, D.D., Kallman, B.R., Bhaskar, S.T., Fleischmann, A., Axel, R., 2011. Driving
484 opposing behaviors with ensembles of piriform neurons. *Cell* 146, 1004–1015.
- 485 Denarie, B., Tangen, T.A., Ekroll, I.K., Rolim, N., Torp, H., Bjästad, T., Lovstakken, L., 2013.
486 Coherent plane wave compounding for very high frame rate ultrasonography of
487 rapidly moving targets. *IEEE Trans. Med. Imaging* 32, 1265–1276.
- 488 Desai, M., Kahn, I., Knoblich, U., Bernstein, J., Atallah, H., Yang, A., Kopell, N., Buckner, R.L.,
489 Graybiel, A.M., Moore, C.I., Boyden, E.S., 2011. Mapping brain networks in awake mice
490 using combined optical neural control and fMRI. *J. Neurophysiol.* 105, 1393–1405.
- 491 Dirnagl, U., Villringer, A., Einhupl, K.M., 1992. In-vivo confocal scanning laser microscopy
492 of the cerebral microcirculation. *J. Microsc.* 165, 147–157.
- 493 Firestein, S., 2001. How the olfactory system makes sense of scents. *Nature* 413, 211–218.
- 494 Franceschini, M.A., Radhakrishnan, H., Thakur, K., Wu, W., Ruvinskaya, S., Carp, S., Boas, D.
495 A., 2010. The effect of different anesthetics on neurovascular coupling. *Neuroimage*
496 51, 1367–1377.
- 497 Franks, K.M., Russo, M.J., Sosulski, D.L., Mulligan, A.A., Siegelbaum, S.A., Axel, R., 2011.
498 Recurrent circuitry dynamically shapes the activation of piriform cortex. *Neuron* 72,
499 49–56.
- 500 Ghosh, S., Larson, S.D., Hefzi, H., Marnoy, Z., Cutforth, T., Dokka, K., Baldwin, K.K., 2011.
501 Sensory maps in the olfactory cortex defined by long-range viral tracing of single
502 neurons. *Nature* 472, 217–220.
- 503 Gurden, H., Uchida, N., Mainen, Z., 2006. Sensory-evoked intrinsic optical signals in the
504 olfactory bulb are coupled to glutamate release and uptake. *Neuron* 52, 335–345.

- Haberly, L.B., 2001. Parallel-distributed processing in olfactory cortex: new insights from
505 morphological and physiological analysis of neuronal circuitry. *Chem. Senses* 26,
506 551–576.
- 507 Isaacson, J.S., 2010. Odor representations in mammalian cortical circuits. *Curr. Opin.*
508 *Neurobiol.* 20, 328–331.
- 509 Johnson, B.A., Leon, M., 2000. Modular representations of odorants in the glomerular layer
510 of the rat olfactory bulb and the effects of stimulus concentration. *J. Comp. Neurol.*
511 422, 496–509.
- 512 Johnson, B.A., Woo, C.C., Leon, M., 1998. Spatial coding of odorant features in the glomerular
513 layer of the rat olfactory bulb. *J. Comp. Neurol.* 393, 457–471.
- 514 Kim, S.G., Ogawa, S., 2012. Biophysical and physiological origins of blood oxygenation
515 level-dependent fMRI signals. *J. Cereb. Blood Flow Metab.* 32, 1188–1206.
- 516 Kleinfeld, D., Mitra, P.P., Helmchen, F., Denk, W., 1998. Fluctuations and stimulus-induced
517 changes in blood flow observed in individual capillaries in layers 2 through 4 of rat
518 neocortex. *Proc. Natl. Acad. Sci. U. S. A.* 95, 15741–15746.
- 519 Lecoq, J., Tiret, P., Najac, M., Shepherd, G.M., Greer, C.A., Charpak, S., 2009. Odor-evoked
520 oxygen consumption by action potential and synaptic transmission in the olfactory
521 bulb. *J. Neurosci.* 29, 1424–1433.
- 522 Litaudon, P., Cattarelli, M., 1996. Olfactory bulb repetitive stimulations reveal non-
523 homogeneous distribution of the inhibitory processes in the rat piriform cortex.
524 *Eur. J. Neurosci.* 8, 21–29.
- 525 Litaudon, P., Amat, C., Bertrand, B., Vigouroux, M., Buonviso, N., 2003. Piriform cortex
526 functional heterogeneity revealed by cellular responses to odours. *Eur. J. Neurosci.*
527 17, 2457–2461.
- 528 Macé, E., Montaldo, G., Cohen, I., Baulac, M., Fink, M., Tanter, M., 2011. Functional ultra-
529 sound imaging of the brain. *Nat. Methods* 8, 662–664.
- 530 Macé, E., Montaldo, G., Osmanski, B.F., Cohen, I., Fink, M., Tanter, M., 2013. Functional
531 ultrasound imaging of the brain: theory and basic principles. *IEEE Trans. Ultrason.*
532 *Ferroelectr. Freq. Control* 60, 492–506.
- 533 Miyamichi, K., Amat, F., Moussavi, F., Wang, C., Wickersham, I., Wall, N.R., Taniguchi, H.,
534 Tasic, B., Huang, Z.J., He, Z., Callaway, E.M., Horowitz, M.A., Luo, L., 2011. Cortical
535 representations of olfactory input by trans-synaptic tracing. *Nature* 472, 191–196.
- 536 Mombaerts, P., 2004. Genes and ligands for odorant, vomeronasal and taste receptors.
537 *Nat. Rev. Neurosci.* 5, 263–278.
- 538 Montaldo, G., Tanter, M., Bercoff, J., Benech, N., Fink, M., 2009. Coherent plane-wave
539 compounding for very high frame rate ultrasonography and transient elastography.
540 *IEEE Trans. Ultrason. Ferroelectr. Freq. Control* 56, 489–506.
- 541 Mori, K., Sakano, H., 2011. How is the olfactory map formed and interpreted in the
542 mammalian brain? *Annu. Rev. Neurosci.* 34, 467–499.
- 543 Mori, K., Takahashi, Y.K., Igarashi, K.M., Yamaguchi, M., 2006. Maps of odorant molecular
544 features in the mammalian olfactory bulb. *Physiol. Rev.* 86, 409–433.
- 545 Murthy, V.N., 2011. Olfactory maps in the brain. *Annu. Rev. Neurosci.* 34, 233–258.
- 546 Osmanski, B.F., Pernot, M., Montaldo, G., Bel, A., Messas, E., Tanter, M., 2012. Ultrafast
547 Doppler imaging of blood flow dynamics in the myocardium. *IEEE Trans. Med. Imaging*
548 31, 1661–1668.
- 549 Pain, F., L'Heureux, B., Gurden, H., 2011. Visualizing odor representation in the brain: a
550 review of imaging techniques for the mapping of sensory activity in the olfactory
551 glomeruli. *Cell. Mol. Life Sci.* 68, 2689–2709.
- 552 Paxinos, G., Watson, C., 2007. *The Rat Brain in Stereotaxic Coordinates*, 6th ed. Academic
553 Press, Elsevier Inc., San Diego.
- 554 Petersen, C.C., 2007. The functional organization of the barrel cortex. *Neuron* 56, 339–355.
- 555 Petzold, G.C., Murthy, V.N., 2011. Role of astrocytes in neurovascular coupling. *Neuron* 71,
556 782–797.
- 557 Petzold, G., Albeanu, D., Sato, T., Murthy, V., 2008. Coupling of neural activity to blood flow
558 in olfactory glomeruli is mediated by astrocytic pathways. *Neuron* 58, 897–910.
- 559 Poo, C., Isaacson, J.S., 2009. Odor representations in olfactory cortex: “sparse” coding,
560 global inhibition, and oscillations. *Neuron* 62, 850–861.
- 561 Poo, C., Isaacson, J.S., 2011. A major role for intracortical circuits in the strength and tuning
562 of odor-evoked excitation in olfactory cortex. *Neuron* 72, 41–48.
- 563 Rennaker, R.L., Chen, C.F., Ruyle, A.M., Sloan, A.M., Wilson, D.A., 2007. Spatial and temporal
564 distribution of odorant-evoked activity in the piriform cortex. *J. Neurosci.* 27, 1534–1542.
- 565 Rubin, B.D., Katz, L.C., 1999. Optical imaging of odorant representations in the mammalian
566 olfactory bulb. *Neuron* 23, 499–511.
- 567 Rubin, J.M., Adler, R.S., Fowlkes, J.B., Spratt, S., Pallister, J.E., Chen, J.F., Carson, P.L., 1995.
568 Fractional moving blood volume: estimation with power Doppler US. *Radiology*
569 197, 183–190.
- 570 Rubin, J.M., Bude, R.O., Fowlkes, J.B., Spratt, R.S., Carson, P.L., Adler, R.S., 1997. Normalizing
571 fractional moving blood volume estimates with power Doppler US: defining a stable
572 intravascular point with the cumulative power distribution function. *Radiology* 205,
573 757–765.
- 574 Saar, D., Barkai, E., 2009. Long-lasting maintenance of learning-induced enhanced
575 neuronal excitability: mechanisms and functional significance. *Mol. Neurobiol.* 576
577 39, 171–177.
- 578 Schuett, S., Bonhoeffer, T., Hübener, M., 2002. Mapping retinotopic structure in mouse visual
579 cortex with optical imaging. *J. Neurosci.* 22, 6549–6559.
- 580 Shepherd, G.M., Greer, C.A., 1998. The olfactory bulb. In: Shepherd, G.M. (Ed.), *The Synaptic*
581 *Organization of the Brain*. Oxford University Press, New York, pp. 159–203.
- 582 Shih, A.Y., Friedman, B., Drew, P.J., Tsai, P.S., Lyden, P.D., Kleinfeld, D., 2009. Active dilation
583 of penetrating arterioles restores red blood cell flux to penumbral neocortex after
584 focal stroke. *J. Cereb. Blood Flow Metab.* 29, 738–751.
- 585 Shung, K.K., Sigelmann, R.A., Reid, J.M., 1976. Scattering of ultrasound by blood. *IEEE*
586 *Trans. Biomed. Eng.* 23, 460–467.
- 587 Sosulski, D.L., Bloom, M.L., Cutforth, T., Axel, R., Datta, S.R., 2011. Distinct representations
588 of olfactory information in different cortical centres. *Nature* 472, 213–216.
- 589 Soucy, E.R., Albeanu, D.F., Fantana, A.L., Murthy, V.N., Meister, M., 2009. Precision and
590 diversity in an odor map on the olfactory bulb. *Nat. Neurosci.* 12, 210–220.

- 591 Stettler, D.D., Axel, R., 2009. Representations of odor in the piriform cortex. *Neuron* 63, 854–864. 609
- 592 610
- 593 Stokes, C.C., Isaacson, J.S., 2010. From dendrite to soma: dynamic routing of inhibition by 611
- 594 complementary interneuron microcircuits in olfactory cortex. *Neuron* 67, 452–465. 612
- 595 Suzuki, N., Bekkers, J.M., 2007. Inhibitory interneurons in the piriform cortex. *Clin. Exp. 613*
- 596 *Pharmacol. Physiol.* 34, 1064–1069. 614
- 597 Suzuki, N., Bekkers, J.M., 2010. Distinctive classes of GABAergic interneurons provide 615
- 598 layer-specific phasic inhibition in the anterior piriform cortex. *Cereb. Cortex* 20, 616
- 599 2971–2984. 617
- 600 Suzuki, N., Bekkers, J.M., 2012. Microcircuits mediating feedforward and feedback synap- 618
- 601 tic inhibition in the piriform cortex. *J. Neurosci.* 32, 919–931. 619
- 602 Tanter, M., Bercoff, J., Athanasiou, A., Deffieux, T., Gennisson, J.L., Montaldo, G., Muller, M., 620
- 603 Tardivon, A., Fink, M., 2008. Quantitative assessment of breast lesion viscoelasticity: 621
- 604 initial clinical results using supersonic shear imaging. *Ultrasound Med. Biol.* 34, 622
- 605 1373–1386. 623
- 606 Thrane, A.S., Rangroo Thrane, V., Zeppenfeld, D., Lou, N., Xu, Q., Nagelhus, E.A., 624
- 607 Nedergaard, M., 2012. General anesthesia selectively disrupts astrocyte calcium 625
- 608 signaling in the awake mouse cortex. *Proc. Natl. Acad. Sci. U. S. A.* 109, 18974–18979. 626
- Uchida, N., Takahashi, Y.K., Tanifuji, M., Mori, K., 2000. Odor maps in the mammalian 609
- olfactory bulb: domain organization and odorant structural features. *Nat. Neurosci.* 610
- 3, 1035–1043. 611
- Udesen, J., Gran, F., Hansen, K.L., Jensen, J.A., Thomsen, C., Nielsen, M.B., 2008. High frame- 612
- rate blood vector velocity imaging using plane waves: simulations and preliminary 613
- experiments. *IEEE Trans. Ultrason. Ferroelectr. Freq. Control* 55, 1729–1743. 614
- Vincis, R., Gschwend, O., Bhaukaurally, K., Beroud, J., Carleton, A., 2012. Dense representation 615
- of natural odorants in the mouse olfactory bulb. *Nat. Neurosci.* 15, 537–539. 616
- Wachowiak, M., Cohen, L.B., 2003. Correspondence between odorant-evoked patterns 617
- of receptor neuron input and intrinsic optical signals in the mouse olfactory bulb. 618
- J. Neurophysiol.* 89, 1623–1639. 619
- Xu, F., Kida, I., Hyder, F., Shulman, R.G., 2000. Assessment and discrimination of odor 620
- stimuli in rat olfactory bulb by dynamic functional MRI. *Proc. Natl. Acad. Sci. U. S. A.* 621
- 97, 10601–10606. 622
- Yoshida, I., Mori, K., 2007. Odorant category profile selectivity of olfactory cortex neurons. 623
- J. Neurosci.* 27, 9105–9114. 624
- Zhan, C., Luo, M., 2010. Diverse patterns of odor representation by neurons in the anterior 625
- piriform cortex of awake mice. *J. Neurosci.* 30, 16662–16672. 626

UNCORRECTED PROOF